

THE SWIFT AGN & CLUSTER SURVEY V:
MEASURING THE AGN ANGULAR CORRELATION FUNCTION

Brett Bonine



The University of Oklahoma

Homer L. Dodge Department of Physics & Astronomy

*A GENERAL EXAMINATION submitted in fulfillment of the
requirements for the DOCTORAL DEGREE*

THE SWIFT AGN & CLUSTER SURVEY V: MEASURING THE AGN ANGULAR CORRELATION FUNCTION

BRETT BONINE¹

¹*Homer L. Dodge Department of Physics & Astronomy, University of Oklahoma, Norman, OK 73019*

Abstract

We present a measurement of the angular clustering of 22,000 X-ray selected AGN from the SWIFT AGN and Cluster survey (SACS), one of the largest medium-depth serendipitous X-Ray surveys to date. To accomplish this, we measured the angular correlation function against random source distributions simulated based on SWIFT XRT exposure maps for 739 fields and then calculated the weighted-average correlation function over all fields. We investigate differences between the clustering of obscured and unobscured AGN by using the MIR blue and MIR red subsamples based on their available *WISE* colors. Finally, we deproject the angular correlation function via Limber's Inversion to infer the real-space clustering properties and the AGN bias.

Keywords: cosmology: large-scale structure of the universe; galaxies: active; surveys; X-rays: galaxies

1. INTRODUCTION

The origin and evolution of large scale structure in the universe remains at the forefront of modern astronomy. As our own solar system is embedded in a galaxy, it is crucial to understand how galaxies such as our own came to be. The finite travel time of light from distant regions of the universe gives astronomers a unique ability to look into the past: light we observe now from structures at cosmological distances was emitted far in the ancient history of the universe. Due to the expansion of the universe, light emitted from these distant objects acquires a characteristic redshift defined to be

$$z = \frac{\lambda_{obs} - \lambda_{rest}}{\lambda_{rest}} \quad (1)$$

Where λ_{obs} and λ_{rest} are the observed and rest-frame wavelengths of light, respectively. The metric expansion of the universe allows us to relate the observed redshift of an object to its distance, and therefore the age of the universe when the light from that object was emitted. Thus, we can study the evolution of structure in the universe by comparing the behavior of structures at progressively higher redshifts.

It has been well established that the majority of large galaxies contain a supermassive black hole (SMBH) at their center (Magorrian et al. 1998). Many studies have found correlations between SMBH

properties and properties of their host galaxies, such as a correlation between SMBH mass and host galaxy bulge mass (McConnell & Ma 2013) and the famous $M - \sigma$ relation that correlates SMBH mass with the velocity dispersion of stars in the host galaxy (Gebhardt et al. 2000). Baes et al. (2003) found evidence that this correlation extends further into the outer reaches of galaxies, suggesting a relationship between the central SMBH and the surrounding dark matter halo. Evidently, studying the growth of SMBHs can give insight into the growth and evolution of their host galaxies. Whenever gas and dust within a galaxy make their way to the central SMBH, inter-particle interactions within the in-falling material causes emission across a broad range of wavelengths. These “active” galactic nuclei (AGN) can therefore be used as signposts for galaxy growth due to their incredible luminosity. Two of the proposed mechanisms for AGN triggering are major mergers (where material can experience gravitational torque from the merger of two galaxies and lose angular momentum) and disk instability (gas inflow due to the instability inherent to a self-gravitating gas) (Oogi et al. 2020). The former mechanism has been thoroughly investigated in the literature and found to be consistent with observations by many analyses, but inconsistent by some others. Hine et al. (2016) investigated the rest-frame UV merger fraction in a $z \approx 3$ protocluster found by Lehmer et al. (2009) to have an overdensity of AGN and determined an elevated fraction of merging galaxies compared to the field. Similarly, Fan et al. (2016) and Glikman et al. (2015) also found elevated merger fractions by studying quasar morphology and brightness profiles. On the contrary, some observations of AGN with moderate X-ray luminosity ($L_x \approx 10^{43} \text{ erg s}^{-1}$) have failed to find evidence of morphologies consistent with major mergers (Kocevski et al. 2012; Cisternas et al. 2011) or enhanced merger fractions of AGN compared to the field (Marian et al. 2019). Thus, the exact mechanism(s) that cause material to migrate to the central SMBH and trigger AGN remains an area of ongoing research.

2. PREVIOUS WORK

Due to the importance of clustering measurements in constraining AGN formation channels, many studies have previously explored the clustering properties of AGN. A direct probe of the AGN environment is the two-point spatial correlation function, where redshift measurements for each AGN are combined with their angular positions on the sky to measure their three-dimensional clustering. In the current Λ -CDM paradigm, “cold” dark matter underwent gravitational collapse into virialized structures early in the history of the universe. As the universe expanded, matter began to cool and occupy the existing dark matter “halos”. The most powerful aspect of the spatial correlation function is its connection to the mass of these dark matter halos (Mo & White 1996). By studying the spatial correlation function of AGN, one can thus probe the environment of typical AGN and place constraints on proposed AGN fueling modes (Krolewski & Eisenstein 2015). Large area optical band redshift surveys such as the Sloan Digital Sky Survey (SDSS) have allowed for precise measurements of the spatial clustering of optically bright luminous AGN (Ross et al. 2009). Because a large volume of redshift measurements are required to measure the spatial correlation function of a sample, many studies instead opt to measure the *angular* correlation function and deproject it using Limber’s inversion (Limber 1953) by making several assumptions about the distribution of true AGN population. The observed clustering properties can either be related to the typical environment of AGN by measuring the AGN bias (Tinker et al. 2005, see below) or compared with the predictions from semi-analytic models of various possible AGN environments. Angular correlation measurements of AGN have been facilitated in recent decades with the help of large-scale X-ray surveys from space-based observatories such as *XMM-Newton*, *Chandra* and *ROSAT*. Elyiv et al. (2012); Ebrero et al. (2009);

Gandhi et al. (2006) inferred the characteristic angular clustering amplitude and slope in both the soft and hard band from serendipitous *XMM-Newton* surveys. Koutoulidis et al. (2016) investigated AGN clustering from hard band *Chandra* data. Miyaji et al. (2011) used an analogous technique involving cross-correlation with galaxies from SDSS. A summary of the measurements made by existing X-ray surveys in the literature is summarized below in Fig. 8. Although measurements of the clustering amplitude θ_0 differ within the literature, clustering measurements of X-ray selected AGN consistently find a higher value of the power-law slope than the canonical value of $\gamma = 1.8$ that has been well established by optical surveys (Peebles 1980).

The clustering AGN have been used to investigate the evolution of AGN properties over cosmic time (Koutoulidis et al. 2013), the formation of SMBHs (Miyaji et al. 2011), and the distribution of density fluctuations at various scales. Of particular interest to this work is the ability to test AGN unification theories by comparing the clustering of obscured and unobscured AGN (Ebrero et al. 2009). Despite assumptions made by the Limber integral equation, Koutoulidis et al. (2016) found consistent results between a direct measurement of the spatial correlation function and a deprojection of the angular correlation function when tested on the same sample of X-ray selected AGN. For this reason, we will investigate use of the angular correlation function in this work.

3. DATA

Our data consist of 22,000 AGN selected from the SWIFT AGN & Cluster Survey (SACS) (Dai et al. 2015). This medium-depth Survey compiled X-ray sources detected in 739 SWIFT GRB fields. AGN candidates were selected as non-extended X-ray sources in the SACS catalog and matched to sources in the Mid IR *WISE* survey. The total sky coverage of the SWIFT GRB fields (125 deg^2) and medium depth of the survey provides a bridge between previous studies of AGN clustering in deep pencil-beam surveys and shallower wide-field surveys. Of the total AGN sample, our dataset contain 17,000 AGN detected in the soft-band (0.2 - 2 keV) and 10,000 detected in the in hard band (2 - 8 keV). The combination of broad X-ray spectral coverage, available MIR colors, large sample size, and survey depth provides us a unique opportunity to investigate the clustering of both obscured and unobscured AGN.

4. METHODOLOGY

A quantity of interest in studying the large-scale structure of AGN is the number overdensity parameter, defined as

$$\delta = \frac{n - \bar{n}}{\bar{n}} \quad (2)$$

where \bar{n} is the average number of AGN found in the sky. It has long been known that AGN do not trace the total distribution of matter in the universe (Bardeen et al. 1986), so it is appropriate to quantify this with a bias parameter b :

$$b = \frac{\delta_{AGN}}{\delta_{DM}} \quad (3)$$

Where δ_{DM} is the overdensity of dark matter halos. In this work, we will use the angular correlation function to infer the real-space clustering properties of our AGN sample. Similar to the definition of the spatial correlation function, the two-point angular correlation function measures the excess

probability that two sources within infinitesimal solid angles $d\omega_1$ and $d\omega_2$ are located at a given angular separation from one another. At small scales, the two-point angular correlation function has been shown to follow a simple power-law behavior:

$$W(\theta) = \left(\frac{\theta}{\theta_0} \right)^{1-\gamma} \quad (4)$$

Where θ_0 is the characteristic angular clustering scale γ is the power-law index. There are multiple methods that can be used to estimate the angular correlation function at various angular scales. In this paper we use the Hamilton Estimator from [Hamilton \(1993\)](#):

$$W(\theta) = N \frac{DD \times RR}{DR^2} - 1 \quad (5)$$

Where DD , RR , and DR are the number of data-data, random-random, and data-random pairs between a real and simulated data set in a given bin of angular separation, respectively. The uncertainty for this estimator is given by

$$\sigma_W = \frac{1 + W}{\sqrt{DD}} \quad (6)$$

Our process for measuring the correlation function is done in two parts: First, we iterate through various exposure maps and use the flux limit of each pixel to generate random sources for that field (see below). Next, we tally the DD , RR , and DR pair counts within each field. So long as there are more than a user-specified number of sources in the field (for this analysis, we assume $N_{cut} = 2$), the correlation function is calculated for that field according to Eq.5 for a user-specified binning scheme. In this work, we take logarithmically spaced bins to a maximum of 1200 arcseconds ($1'' = \frac{1}{3600}^\circ$). Pair counts at a separation smaller than $18''$ would not be resolvable due to the SWIFT XRT's point-spread function (PSF) size of $17.35''$, so we do not consider angular scales smaller than this in our analysis. Finally, we clean out bins with no data and evaluate the weighted average correlation function in each bin according to

$$\bar{W} = \frac{\sum_{i=1}^n \left(\frac{W_i}{\sigma_i^2} \right)}{\sum_{i=1}^n \frac{1}{\sigma_i^2}} \quad (7)$$

The standard error of each weighted mean is given by

$$\sigma_{\bar{W}_i} = \sqrt{\frac{1}{\sum_{i=1}^n \sigma_i^{-2}}} \quad (8)$$

4.1. RANDOM CATALOG GENERATION

To generate the random catalogs for this analysis, we follow a modified version of the “sensitivity map” procedure outlined in Koutoulidis et al. (2013). We begin by reading in the SWIFT XRT exposure maps for each SACS GRB field. The exposure time of a given pixel in the map can be directly related to a flux limit associated with that exposure time and therefore a sensitivity. Once we determine the flux limit of every pixel in the exposure map, we use the differential number counts statistic to infer the expected number of sources per pixel. The differential number counts are given by

$$\frac{dN}{dS} = \begin{cases} K(S/S_{ref})^{-a} & (S \leq f_b) \\ K(f_b/S_{ref})^{b-a} & (S > f_b) \end{cases} \quad (9)$$

where f_b is flux associated with the power law break, S_{ref} is a reference flux, and K , b , and a are fit parameters associated with the normalization and power law indices, respectively. We adopt the values of the power law fit from Dai et al. (2015) for this analysis. To find the cumulative number counts ($N > S$), we integrate Eq. 9 from the flux limit of the pixel to infinity. This can be analytically expressed as

$$N(> S) = \begin{cases} -K\left(\frac{1}{-a+1}\right)\left(\frac{1}{S_{ref}}\right)^{-a} f_b^{-a+1} s^{-a+1} & (S \leq f_b) \\ -K\left(\frac{f_b}{S_{ref}}\right)^{b-a} \left(\frac{1}{-b+1}\right)\left(\frac{1}{S_{ref}}\right)^{-b} f_b^{-b+1} s^{-b+1} & (S > f_b) \end{cases} \quad (10)$$

The relative pixel values of each exposure map are used to make a weight-map that describes the likelihood of a given pixel in a synthetic image having a source. To place the sources inferred by the integrated differential source count, we draw N values from a uniform distribution between zero and the total weight of the weight-map. We then iterate through each pixel of the exposure map and compare the value of the draw to that pixel’s associated boundaries in the weight-map. If the draw falls within the weight-map boundaries for that pixel, we update the value of the associated pixel to be non-zero in an associated random image. Finally, we record the X and Y positions of all non-zero pixels in the random image and move on to the next field.

As a test of the accuracy of our integration, we plot the number of sources against the mean exposure map value (a proxy for exposure time) for both the real and simulated sources. As evident in Fig 4.1, the number of random sources scales comparably with the number of real sources. Thus, our technique for estimating the number of sources in each field by integrating Eq. 9 is reliable.

5. TESTING THE 2PACF ALGORITHM

In order to make sure the random catalogs generated are accurate and we are calculating the correlation function correctly, we first test the correlation function algorithm on two separately generated random catalogs, i.e., one of the two random catalogs is arbitrarily labeled as “data” and compared against the other. The expected result for this procedure is $W(\theta) \approx 0$ for all angular scales. As shown in Fig 5, our algorithm produces a result consistent with this for most angular scales, suggesting that any signal that arises in a calculation with the real dataset will be physical.

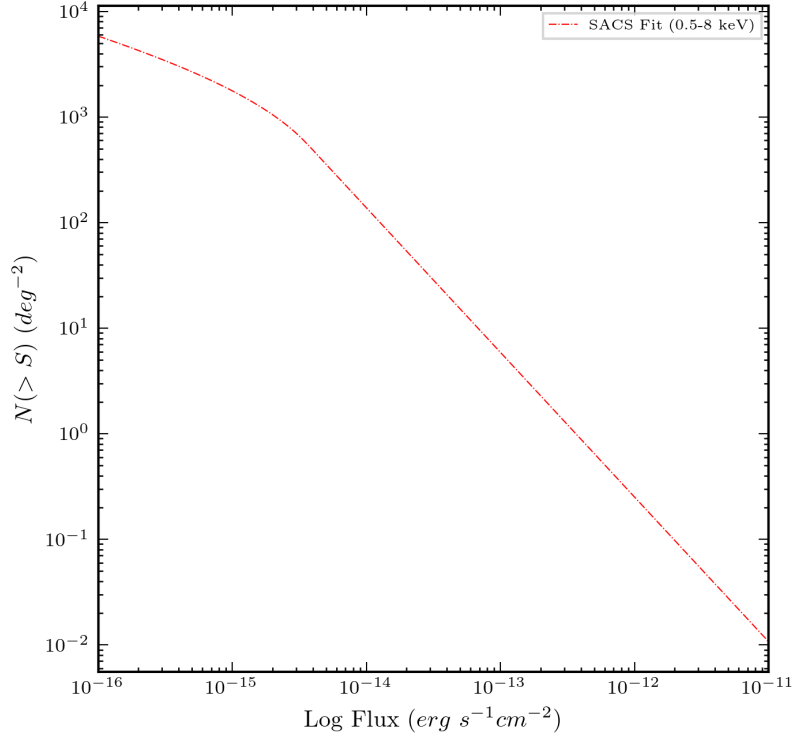


Figure 1. Cumulative source count vs. Flux Limit for the simulated AGN (red dashed line) from integrating Eq. 9. This plot shows the number of AGN (per square degree) that should be detectable for a given flux limit. Given that the the SWIFT XRT has a pixel scale of $2.36''$ per pixel, we can use this graph to estimate the number of AGN that should appear in a random image.

6. RESULTS: 2PACF ON SACS DATASET

6.1. Complete Sample

After determining that our algorithm was performing as expected, we repeat the correlation analysis above using the SACS AGN catalog as our dataset. Each field contains an average of 30 AGN, though we disregard fields that contain less than two real or rand points. After calculating the weighted average correlation function, we use the software package *Sherpa* (Freeman et al. 2001) to fit a powerlaw to the measurement. We find a slope of $\gamma = 2.07 \pm 0.087$ and a clustering amplitude of $\theta_0 = 8.18 \pm 3.11$ for the complete dataset. The clustering amplitude is consistent with the findings of Elyiv et al. (2012) while our slope more closely matches that of Ebrero et al. (2009), whose softband analysis featured a slightly larger AGN catalog than our own.

6.2. Obscured vs Unobscured Subsample

The canonical picture of AGN unification attributes the differences in observed AGN spectral type (Type I or Type II) to the viewing angle of the observer (Antonucci & Miller 1985). If this model is correct, then both Type I and Type II AGN should have similar host halo mass distributions and therefore cluster similarly on the sky (Mitra et al. 2018). To test this, we divide our samples of SACS

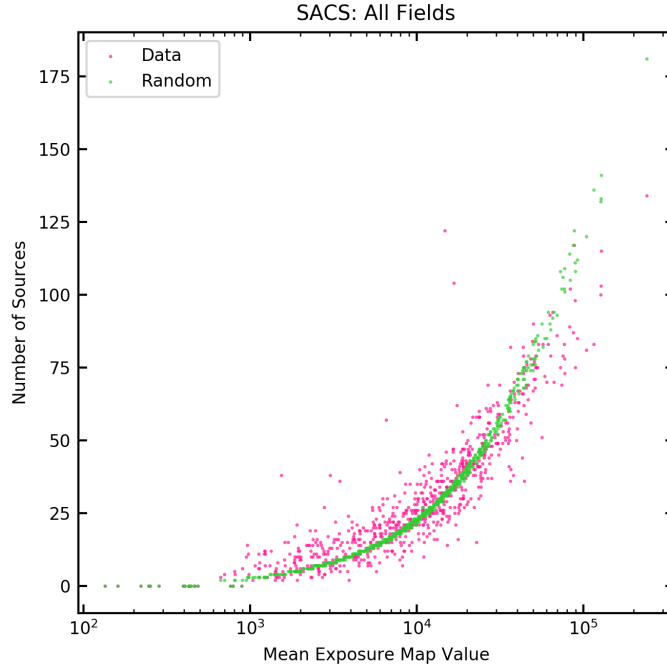


Figure 2. Number of sources vs Mean Exposure Map Value for all 739 fields. The number of simulated sources evolves similarly to the number of real sources with increasing exposure time, suggesting our analytic integration of the power-law differential source count is accurate. Note that the scatter of the data is larger than the simulation.

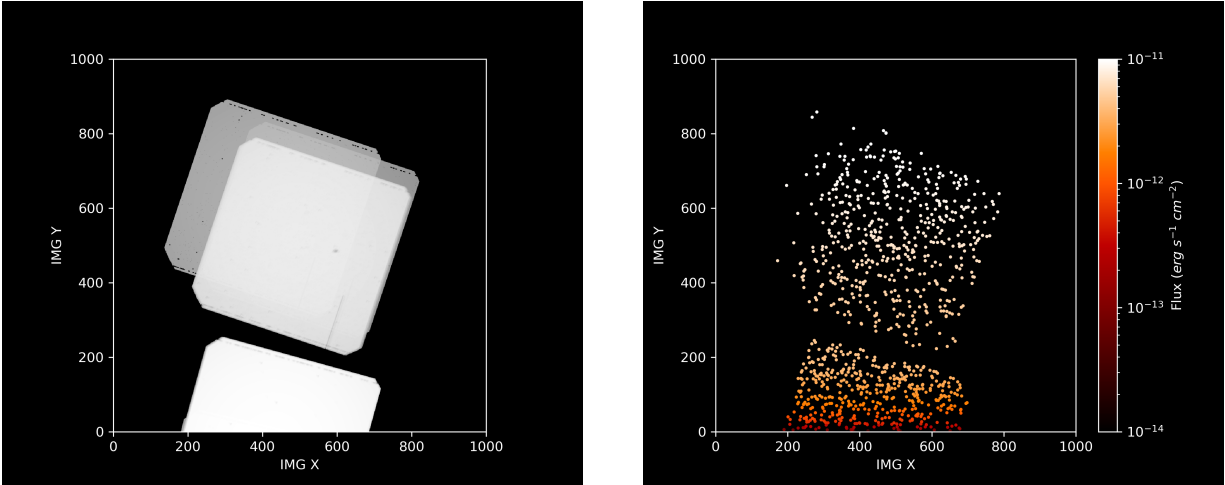


Figure 3. A sample exposure map from one of the 739 SACS grb fields (left) and the associated random image (right). The number of random sources is 100 times the number of real sources observed in this particular field. Each source is color-coded by a flux drawn from the observed log N - log S distribution.

AGN into “MIR red” and “MIR blue” using the scheme from [Dai et al. \(2015\)](#). We label AGN with $W1 - W2 \leq 0.35$ mag MIR blue and those with color $W1 - W2 > 0.35$ as MIR red. Using this criteria, the fraction of obscured and unobscured AGN are $f_{blue} = 0.53$, $f_{red} = 0.47$, respectively.

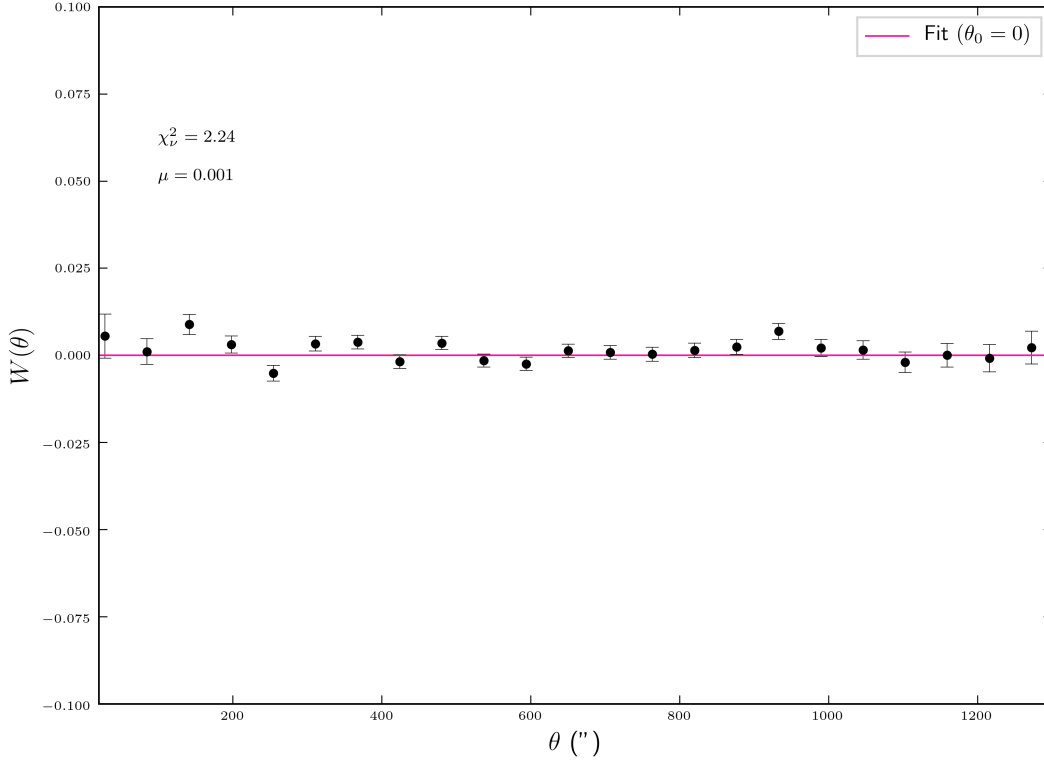


Figure 4. Two-Point Angular Correlation Function evaluated between two random catalogs. The result is mostly consistent with no correlation, as expected.

Table 1. Best Fit Values

Sample	θ_0 (")	γ	χ^2_ν
SACS All	8.14 ± 3.11	2.07 ± 0.087	0.75
MIR Red	32.02 ± 11.26	2.16 ± 0.058	1.08
MIR Blue	28.65 ± 8.35	2.11 ± 0.049	1.57

Our procedure for investigating the color dependence of the angular correlation function is as follows: We construct a new random catalog following the original procedure, but this time generate two random images per field. The number of random sources in each image is the expected result from the procedure in section 4 multiplied by f_{blue} and f_{red} for the blue and red AGN, respectively. Next we repeat the correlation analysis described in Section 3 for the two subsamples separately. For the blue subsample, we find a powerlaw slope of $\gamma_b = 2.11 \pm 0.049$ and a clustering scale of $\theta_{0,b} = 28.65 \pm 8.35''$. For the red AGN subsample, we measure $\gamma_r = 2.16 \pm 0.058$ and $\theta_{0,r} = 32.02 \pm 11.26$.

7. DEPROJECTING THE ANGULAR CORRELATION FUNCTION

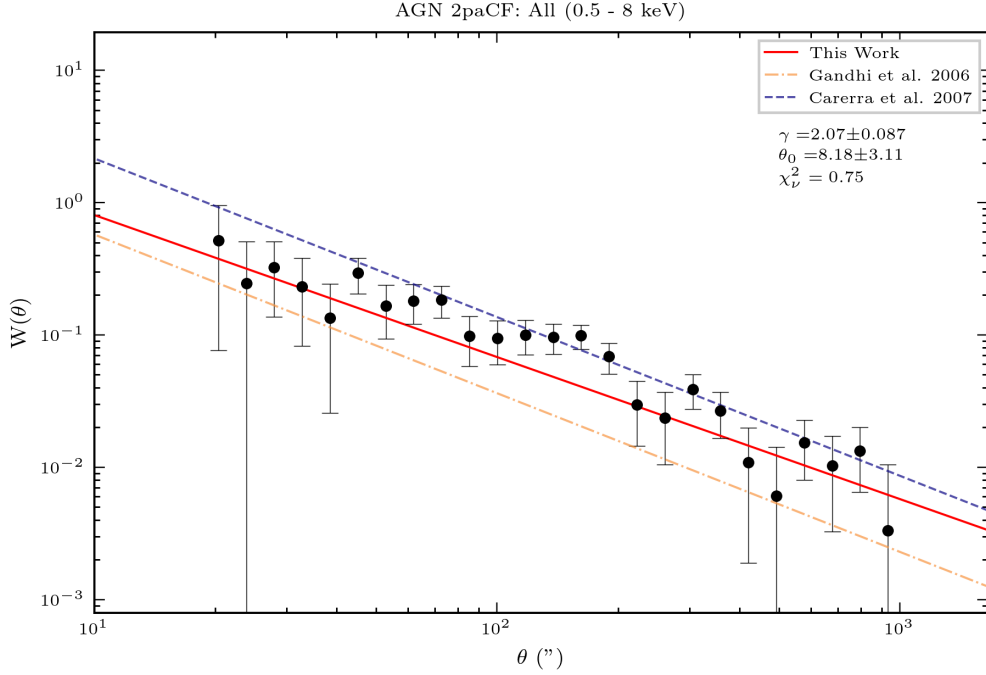


Figure 5. Two-Point Angular Correlation Functions for the the complete SACS AGN sample. Though there are many neagive values for small angular scales, we find a powerlaw behavior consistent with previous results in the literature

Our observed clustering signal is a projection of the true three dimensional clustering of the AGN population. As discussed above, we can infer the true clustering properties by deprojecting our angular measurement. Our primary tool for investigating the real space properties of AGN from the angular correlation function is Limber’s Inversion Equation (Limber 1953). From Koutoulidis et al. (2016), this integral equation can be expressed in terms of observable properties as :

$$\theta_0^{\gamma-1} = H_\gamma x_0^\gamma \int_0^\infty \left(\frac{1}{N} \frac{dN}{dz} \right)^2 \frac{d_A(z)^{1-\gamma}}{cd\tau(z)/dz} \tilde{b}^2(z) \tilde{D}^{2+n}(z) dz \quad (11)$$

where H_γ is related to the gamma function and the powerlaw index of the measured angular correlation function by

$$H_\gamma = \frac{\Gamma\left(\frac{1}{2}\right) \Gamma\left(\frac{\gamma-1}{2}\right)}{\Gamma\left(\frac{\gamma}{2}\right)} \quad (12)$$

The remaining terms are various cosmological parameters related to the angular diameter distance (d_A), growing mode of linear perturbations (\tilde{D}) and the lookback time ($d\tau/dz$). Of interest to this analysis is the normalized bias parameter \tilde{b} , defined in Koutoulidis et al. (2016) as the bias parameter b normalized to its value at $z = 0$:

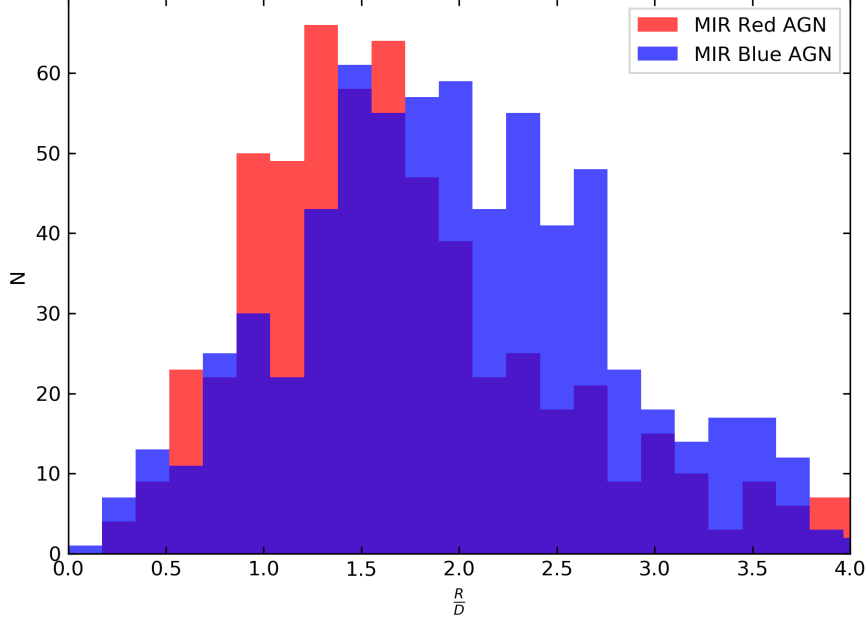


Figure 6. Histogram showing the ratio of N_{rand} to N_{data} for all fields with $N_{data}, N_{rand} > 2$. To reduce shot noise, we multiply the expected number of random sources by a factor two. The means of both distributions are similar but differ slightly due to the different fractions of MIR red and MIR blue AGN in our dataset.

$$\tilde{b}(z) = \frac{b(z)}{b(0)} \quad (13)$$

Where the AGN bias from Eq. 3 can be related to underlying cosmological parameters according to

$$b(z) = 1 + \frac{b_0 - 1}{D(z)} + C_2 \frac{J(z)}{D(z)} \quad (14)$$

The b_0 and C_2 terms are ultimately related to the host dark matter halo mass by

$$b_0(M_h) = 0.857 \left[1 + \left(\frac{\Omega_{m,0}}{0.27} \frac{M_h}{10^{14} h^{-1} M_\odot} \right)^{0.55} \right] \quad (15)$$

$$C_2(M_h) = 1.105 \left[1 + \left(\frac{\Omega_{m,0}}{0.27} \frac{M_h}{10^{14} h^{-1} M_\odot} \right)^{0.255} \right] \quad (16)$$

where $\Omega_{m,0}$ is the fractional matter density in the local universe and h is the “ignorance parameter” [Hogg \(1999\)](#) related to the Hubble Constant as

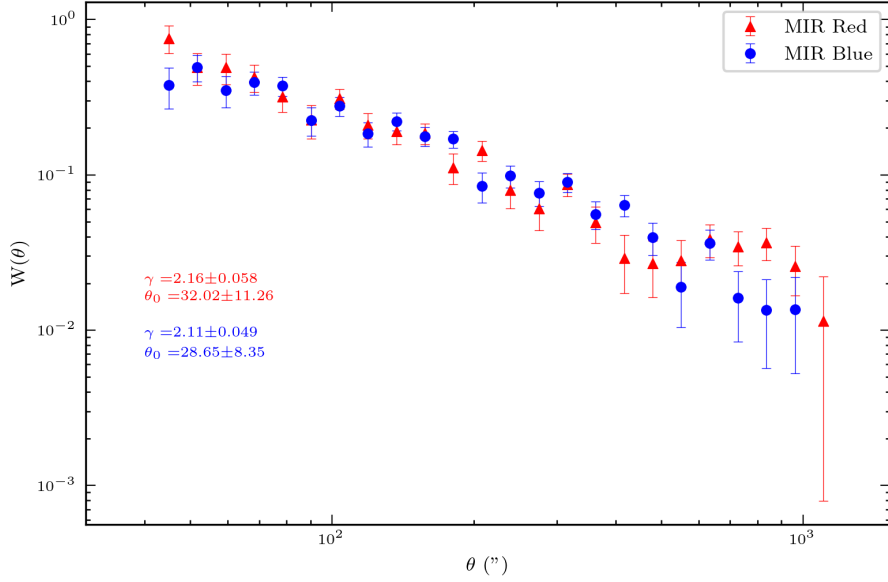


Figure 7. Two-Point Angular Correlation Functions for the MIR Red and MIR Blue AGN subsamples. The clustering amplitude and slope are slightly larger for the MIR Blue AGN in our sample. There is little difference in the clustering of the subsamples at most angular scales.

$$H_0 = 100h \text{ km s}^{-1} \text{ Mpc}^{-1} \quad (17)$$

In the future it may be worth performing our own fits for the characteristic host halo mass, but for now we'll adopt the value assumed by Koutoulidis et al. (2016) ($M_h = 1.3 \times 10^{13} M_\odot$). To deproject our measurement, we need to know the average number of AGN contained within the average solid angle subtended by our fields at each infinitesimal redshift slice:

$$\frac{dN}{dz} = \Omega_s d_A(z)^2 (1+z)^2 \phi(z) \left(\frac{c}{H_0} \right) \frac{1}{E(z)} \quad (18)$$

Where $\phi(z)$ describes the probability that a source at a particular redshift will be observed. This quantity depends on the redshift distribution of the AGN in our sample. Since we don't have redshift information we must assume an X-ray luminosity function $\Phi(L, z)$ to infer $\phi(z)$ according to

$$\phi(z) = \int_{L_{min(z)}}^{\infty} \Phi(L, z) dL \quad (19)$$

where $L_{min(z)}$ is the minimum luminosity we can observe at a particular redshift. We can determine the minimum detectable luminosity at each redshift slice by performing a k -correction to account for the expansion of the universe on the standard flux-luminosity-distance relationship:

$$\bar{f}_{\nu,min} = \frac{L_{\nu,min}(1+z)^{1-\alpha}}{4\pi D_L^2} \quad (20)$$

Where $\bar{f}_{\nu,min}$ is the mean flux limit of our survey and D_L is the luminosity distance to a source at a redshift z . In the future we'll adopt more modern values for the AGN luminosity function, but for now we'll assume the same Luminosity and Density Evolution (LADE) luminosity function used by Koutoulidis et al. (2016) (Aird et al. 2010). A sample of the luminosity function (evaluated at a random redshift of $z = 0.1$) is shown below in Fig 7.

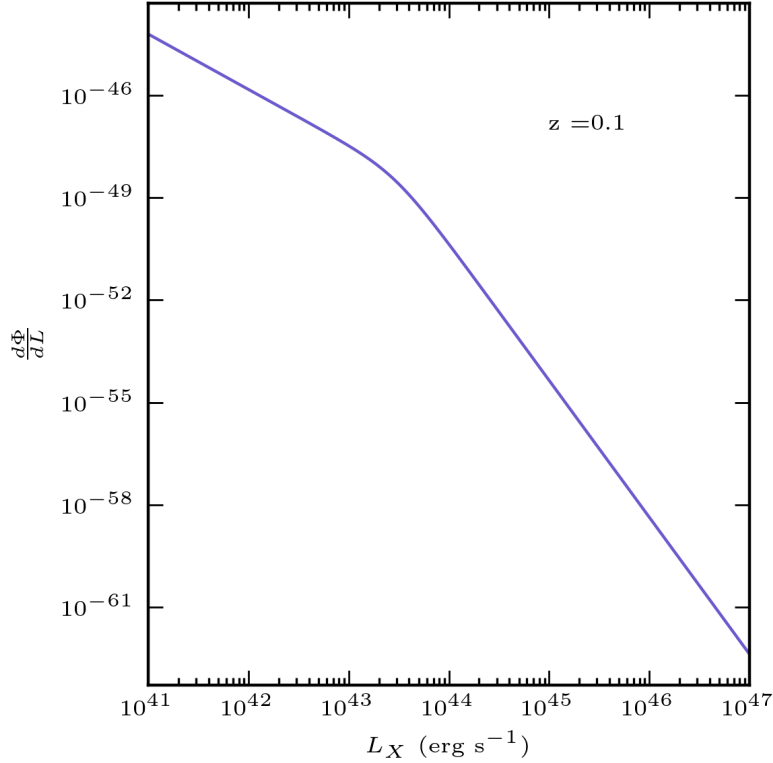


Figure 8. The LADE Luminosity function (with parameters from Aird et al. (2010)) used for deprojecting the angular correlation function in our analysis, shown here evaluated at a redshift of $z = 0.1$. This function can be integrated to infer the number of observable AGN density (per cm^{-3}) for a given minimum observable luminosity.

For our slope of $\gamma = 2.07$, we find a comoving clustering length at of $x_0 = 10.64h^{-1} \text{ Mpc}^{-1}$. Since Limber's Inversion is normalized to the local universe ($z=0$), we can find the clustering length at a particular redshift (in comoving coordinates) according to

$$x_0(z) = x_0(0)\tilde{D}^{2+n/\gamma}(z)\tilde{b}^{2/\gamma} \quad (21)$$

Normalizing our clustering length to the mean of our redshift distribution in Fig. (7), ($z \approx 0.75$), we find a comoving clustering length of $x_0 = 15.39h^{-1}\text{Mpc}^{-1}$.

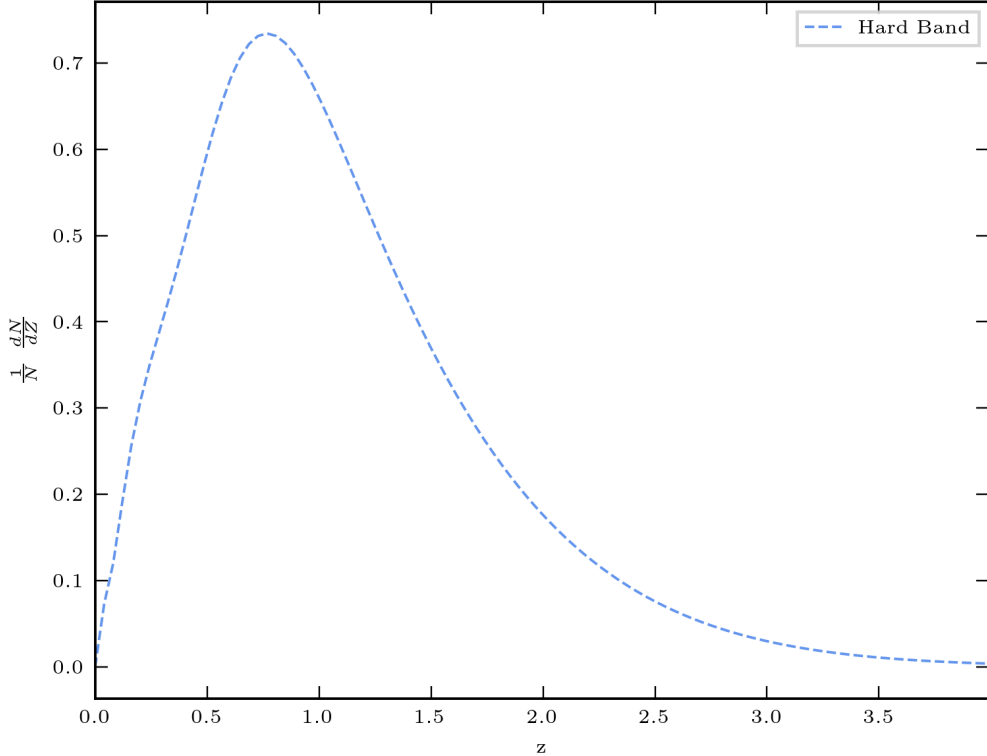


Figure 9. The AGN redshift selection function of our sample inferred by integrating the above luminosity function over all redshifts. The shape of our selection function matches that of the estimated selection function of [Ebrero et al. \(2009\)](#) and is in reasonable agreement with the observed AGN redshift distribution of [Plionis et al. \(2018\)](#).

8. DISCUSSION

For the complete dataset, our measurement of the correlation function is in strong agreement with other soft-band X-Ray surveys in the literature (see Fig. (8)). The calculated angular clustering amplitude sits between the measurement of [Ebrero et al. \(2009\)](#), whose analysis featured a similarly sized dataset, and [Elyiv et al. \(2012\)](#). The measured slope of our dataset agrees strongly with that of the slope found by [Ebrero et al. \(2009\)](#) in the softband. When splitting sample by MIR color, we find similar values for the slope of the angular correlation function for both obscured and unobscured AGN. The best fit clustering amplitude is notably larger for the two subsamples compared to the complete sample (but more in line with the larger amplitudes found by [Ebrero et al. \(2009\)](#) in the soft band). The slopes and clustering amplitudes of the two subsamples are in close agreement at most angular scales, consistent with the findings of the hardness-ratio analysis of [Ebrero et al. \(2009\)](#) and unification models of AGN. Thus a separate metric for splitting the complete sample into obscured and unobscured AGN found no strong difference between the two subsamples' clustering properties.

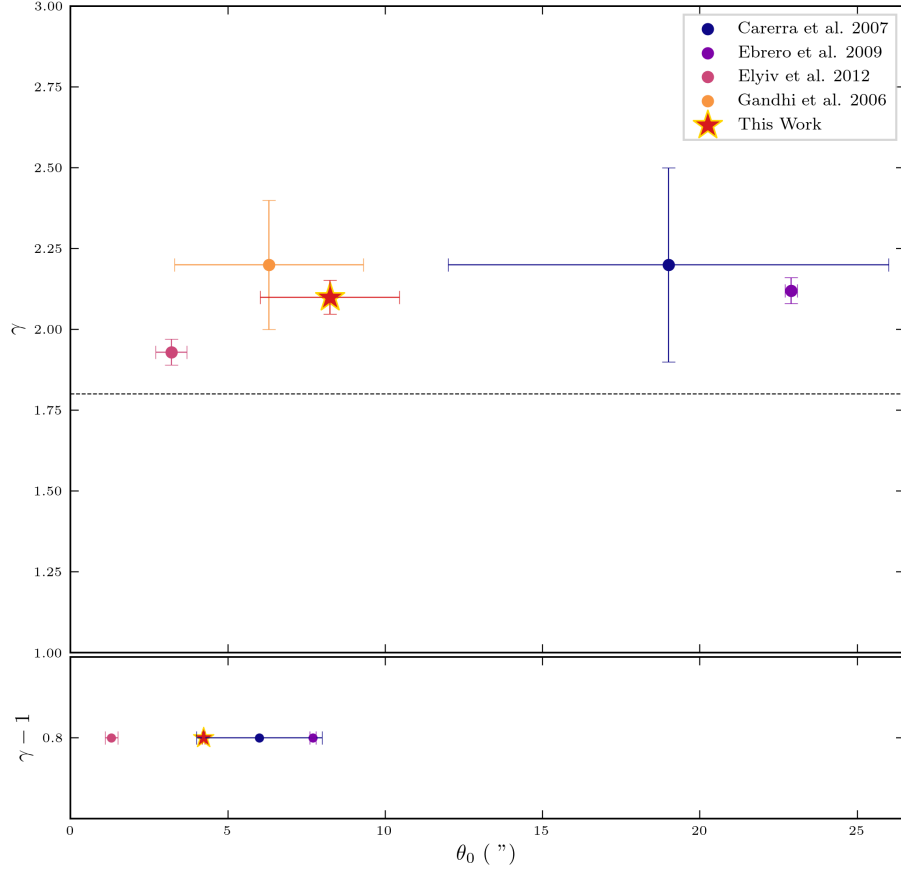


Figure 10. A summary of our contribution to the literature. *Top:* Measurements for γ and θ_0 from other soft-band X-ray survey measurements. The canonical galaxy value of $\gamma = 1.8$ is plotted as the dashed black line, indicating that X-ray selected AGN are not well characterized by this slope. *Bottom* The above results when fit to a value of $\gamma = 1.8$. From Limber’s Inversion, real-space and angular correlation functions are related by $w(\theta) \propto \xi^{\gamma-1}$. Reporting the powerlaw fit of the angular correlation function with fixed slope of $\gamma - 1 = 0.8$ is common in the literature.

The canonical picture of AGN unification discussed above is also known as “unification by orientation.” Although this has been thoroughly investigated in the literature, there are some open issues with this unification scheme that have yet to be explained (see [Netzer \(2015\)](#) for a comprehensive review of AGN unification schemes). An alternative unification scheme discussed in the literature is “unification by evolution,” where different AGN spectral types are really the same phenomena observed at different epochs in their lifetimes, regardless of viewing angle. For this unification scheme, one would expect the distribution of different AGN types to evolve with redshift due to the increasing look-back time with redshift. Since our measurement of the correlation function relies only on the angular positions of obscured and unobscured AGN and not on their redshift, we would be unable to identify differences in the clustering of these two populations for this unification scheme.

Direct measurements of the clustering of optically selected AGN have found a physical clustering lengths on the order of $r_0 \approx 5.4 - 8.6 h^{-1} \text{Mpc}^{-1}$ (Akylas et al. 2000; Croom et al. 2002; Grazian et al. 2004). Similar surveys of X-ray selected AGN have inferred a slightly higher spatial clustering length in the range of $r_0 \approx 7.5 - 9.8 h^{-1} \text{Mpc}^{-1}$ (Basilakos et al. 2008; Miyaji et al. 2011; Plionis et al. 2018). To compare our result to those reported in the literature, we'll express the clustering length in proper coordinates according to

$$r_0 = \left(\frac{x_0}{1+z} \right) \quad (22)$$

Our estimate of the comoving clustering length at $z = 0.75$ translates to a physical distance of $r_0 = 8.79 h^{-1} \text{Mpc}$, in excellent agreement with the above measurements as well as the inferred spatial clustering length of Ebrero et al. (2009).

9. CONCLUSION

In this work we measured the average two-point angular correlation function for 22,000 X-ray selected AGN. Our dataset provides a bridge between previous high depth narrow surveys and shallow wide-field soft-band x-ray surveys. We find an angular clustering amplitude and slope consistent with previous results for the soft-band in the literature, suggesting the clustering of AGN behaves as expected for the AGN population not sampled by previous surveys. We find no statistically significant difference in the clustering amplitude or slope for the obscured or unobscured subsamples, consistent with unification models of AGN. With the exception of large sample size of Ebrero et al. (2009), our analysis comprises one of the most tightly constrained measurements of the angular clustering of AGN to date.

As a final demonstration of the utility of the angular correlation function, we deproject our measurement to find a clustering length in good agreement with the literature. Additional analysis prior to publication may include a comparison of the clustering for different flux-limited subsamples as well as a separate clustering analysis for available SACS hard band (2-8 keV) data. As a followup to Migkas et al. (2020), who found an anisotropy in the galaxy cluster $L_x - T$ relation, it may also be worth investigating the directional dependence of the clustering properties of our sample as a long term goal.

REFERENCES

- | | |
|---|--|
| <p>Aird, J., Nandra, K., Laird, E. S., et al. 2010, MNRAS, 401, 2531, doi: 10.1111/j.1365-2966.2009.15829.x</p> <p>Akylas, A., Georgantopoulos, I., & Plionis, M. 2000, MNRAS, 318, 1036, doi: 10.1046/j.1365-8711.2000.03682.x</p> <p>Antonucci, R. R. J., & Miller, J. S. 1985, ApJ, 297, 621, doi: 10.1086/163559</p> <p>Baes, M., Buyle, P., Hau, G. K. T., & Dejonghe, H. 2003, MNRAS, 341, L44, doi: 10.1046/j.1365-8711.2003.06680.x</p> | <p>Bardeen, J. M., Bond, J. R., Kaiser, N., & Szalay, A. S. 1986, ApJ, 304, 15, doi: 10.1086/164143</p> <p>Basilakos, S., Plionis, M., & Ragone-Figueroa, C. 2008, The Astrophysical Journal, 678, 627, doi: 10.1086/586725</p> <p>Cisternas, M., Jahnke, K., Inskip, K. J., et al. 2011, ApJ, 726, 57, doi: 10.1088/0004-637X/726/2/57</p> <p>Croom, S. M., Boyle, B. J., Loaring, N. S., et al. 2002, MNRAS, 335, 459, doi: 10.1046/j.1365-8711.2002.05639.x</p> |
|---|--|

- Dai, X., Griffin, R. D., Kochanek, C. S., Nugent, J. M., & Bregman, J. N. 2015, *ApJS*, 218, 8, doi: [10.1088/0067-0049/218/1/8](https://doi.org/10.1088/0067-0049/218/1/8)
- Ebrero, J., Mateos, S., Stewart, G. C., Carrera, F. J., & Watson, M. G. 2009, *A&A*, 500, 749, doi: [10.1051/0004-6361/200911670](https://doi.org/10.1051/0004-6361/200911670)
- Elyiv, A., Clerc, N., Plionis, M., et al. 2012, *A&A*, 537, A131, doi: [10.1051/0004-6361/201117983](https://doi.org/10.1051/0004-6361/201117983)
- Fan, L., Han, Y., Fang, G., et al. 2016, *ApJL*, 822, L32, doi: [10.3847/2041-8205/822/2/L32](https://doi.org/10.3847/2041-8205/822/2/L32)
- Freeman, P., Doe, S., & Siemiginowska, A. 2001, in *Society of Photo-Optical Instrumentation Engineers (SPIE) Conference Series*, Vol. 4477, *Astronomical Data Analysis*, ed. J.-L. Starck & F. D. Murtagh, 76–87, doi: [10.1117/12.447161](https://doi.org/10.1117/12.447161)
- Gandhi, P., Garcet, O., Disseau, L., et al. 2006, *A&A*, 457, 393, doi: [10.1051/0004-6361:20065284](https://doi.org/10.1051/0004-6361:20065284)
- Gebhardt, K., Bender, R., Bower, G., et al. 2000, *ApJL*, 539, L13, doi: [10.1086/312840](https://doi.org/10.1086/312840)
- Glikman, E., Simmons, B., Mailly, M., et al. 2015, *ApJ*, 806, 218, doi: [10.1088/0004-637X/806/2/218](https://doi.org/10.1088/0004-637X/806/2/218)
- Grazian, A., Negrello, M., Moscardini, L., et al. 2004, *AJ*, 127, 592, doi: [10.1086/380925](https://doi.org/10.1086/380925)
- Hamilton, A. J. S. 1993, *ApJ*, 417, 19, doi: [10.1086/173288](https://doi.org/10.1086/173288)
- Hine, N. K., Geach, J. E., Alexander, D. M., et al. 2016, *MNRAS*, 455, 2363, doi: [10.1093/mnras/stv2448](https://doi.org/10.1093/mnras/stv2448)
- Hogg, D. W. 1999, arXiv e-prints, astro. <https://arxiv.org/abs/astro-ph/9905116>
- Kocevski, D. D., Faber, S. M., Mozena, M., et al. 2012, *ApJ*, 744, 148, doi: [10.1088/0004-637X/744/2/148](https://doi.org/10.1088/0004-637X/744/2/148)
- Koutoulidis, L., Plionis, M., Georgantopoulos, I., & Fanidakis, N. 2013, *MNRAS*, 428, 1382, doi: [10.1093/mnras/sts119](https://doi.org/10.1093/mnras/sts119)
- Koutoulidis, L., Plionis, M., Georgantopoulos, I., et al. 2016, *A&A*, 590, A23, doi: [10.1051/0004-6361/201527814](https://doi.org/10.1051/0004-6361/201527814)
- Krolewski, A. G., & Eisenstein, D. J. 2015, *ApJ*, 803, 4, doi: [10.1088/0004-637X/803/1/4](https://doi.org/10.1088/0004-637X/803/1/4)
- Lehmer, B. D., Alexander, D. M., Chapman, S. C., et al. 2009, *MNRAS*, 400, 299, doi: [10.1111/j.1365-2966.2009.15449.x](https://doi.org/10.1111/j.1365-2966.2009.15449.x)
- Limber, D. N. 1953, *ApJ*, 117, 134, doi: [10.1086/145672](https://doi.org/10.1086/145672)
- Magorrian, J., Tremaine, S., Richstone, D., et al. 1998, *AJ*, 115, 2285, doi: [10.1086/300353](https://doi.org/10.1086/300353)
- Marian, V., Jahnke, K., Mechtley, M., et al. 2019, *ApJ*, 882, 141, doi: [10.3847/1538-4357/ab385b](https://doi.org/10.3847/1538-4357/ab385b)
- McConnell, N. J., & Ma, C.-P. 2013, *ApJ*, 764, 184, doi: [10.1088/0004-637X/764/2/184](https://doi.org/10.1088/0004-637X/764/2/184)
- Migkas, K., Schellenberger, G., Reiprich, T. H., et al. 2020, *A&A*, 636, A15, doi: [10.1051/0004-6361/201936602](https://doi.org/10.1051/0004-6361/201936602)
- Mitra, K., Chatterjee, S., DiPompeo, M. A., Myers, A. D., & Zheng, Z. 2018, *MNRAS*, 477, 45, doi: [10.1093/mnras/sty556](https://doi.org/10.1093/mnras/sty556)
- Miyaji, T., Krumpke, M., Coil, A. L., & Aceves, H. 2011, *ApJ*, 726, 83, doi: [10.1088/0004-637X/726/2/83](https://doi.org/10.1088/0004-637X/726/2/83)
- Mo, H. J., & White, S. D. M. 1996, *MNRAS*, 282, 347, doi: [10.1093/mnras/282.2.347](https://doi.org/10.1093/mnras/282.2.347)
- Netzer, H. 2015, *ARA&A*, 53, 365, doi: [10.1146/annurev-astro-082214-122302](https://doi.org/10.1146/annurev-astro-082214-122302)
- Oogi, T., Shirakata, H., Nagashima, M., et al. 2020, *MNRAS*, 497, 1, doi: [10.1093/mnras/staa1961](https://doi.org/10.1093/mnras/staa1961)
- Peebles, P. J. E. 1980, *The large-scale structure of the universe*
- Plionis, M., Koutoulidis, L., Koulouridis, E., et al. 2018, *A&A*, 620, A17, doi: [10.1051/0004-6361/201832970](https://doi.org/10.1051/0004-6361/201832970)
- Ross, N. P., Shen, Y., Strauss, M. A., et al. 2009, *ApJ*, 697, 1634, doi: [10.1088/0004-637X/697/2/1634](https://doi.org/10.1088/0004-637X/697/2/1634)
- Tinker, J. L., Weinberg, D. H., Zheng, Z., & Zehavi, I. 2005, *ApJ*, 631, 41, doi: [10.1086/432084](https://doi.org/10.1086/432084)

APPENDIX

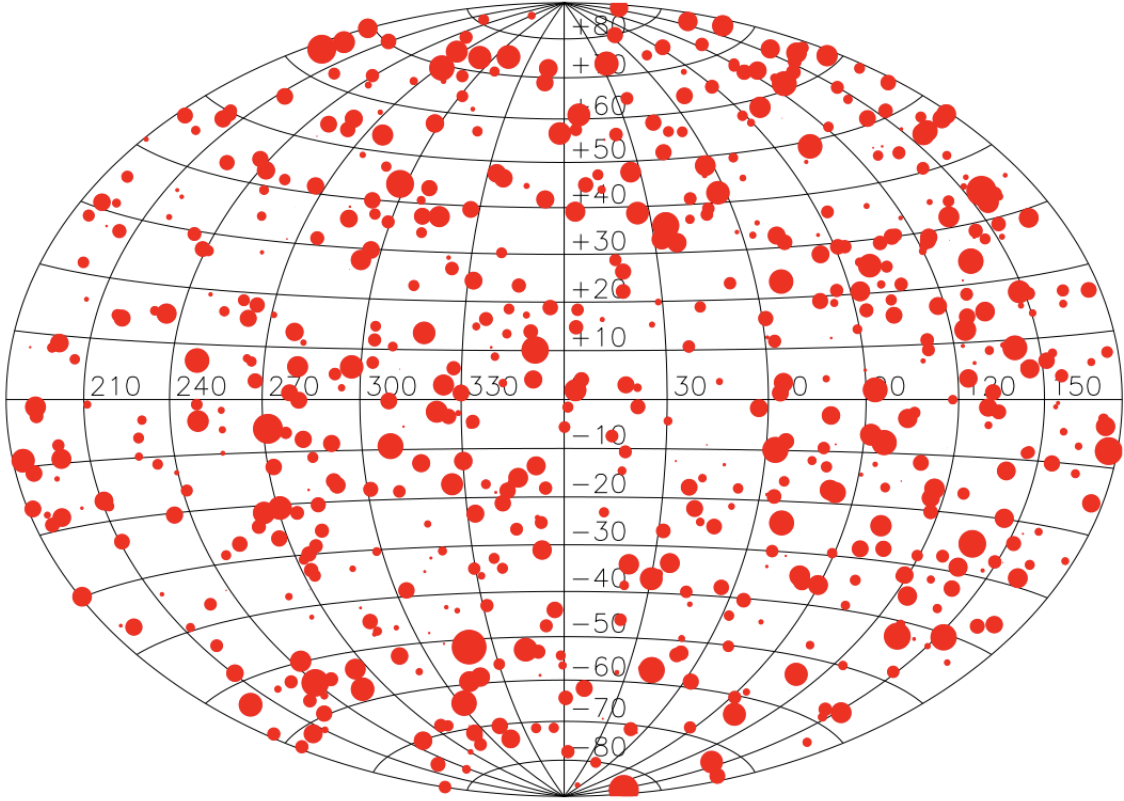


Figure 11. The sky coverage of the 739 fields in SACS. In this work we evaluated the angular correlation function in each one of these fields to infer the average angular correlation function in a region of the sky similar to each pointing above. The large sky coverage of this survey and its total area ($\approx 125^\circ$) help to reduce bias introduced by only sampling an over-dense or under-dense region. Adapted from [Dai et al. \(2015\)](#).